

# Thermal Conductivity Analysis of Compacted Graphite Cast Iron After a Creep Test



WU YUE, LI JIANPING, YANG ZHONG, GUO YONGCHUN, MA ZHIJUN,  
LIANG MINXIAN, YANG TONG, and TAO DONG

The thermal conductivity of compacted graphite cast iron (CGI) after creep test (temperature ranging from 350 °C to 550 °C; stress ranging from 40 to 150 MPa) was measured at different testing temperatures (200 °C to 550 °C) in an argon atmosphere. The thermal conductivity increased slightly when the creep temperature increased from 350 °C to 500 °C under 150 MPa and then decreased dramatically when the creep temperature surpassed 500 °C. When the creep temperature was 550 °C, the thermal conductivity initially decreased slightly, and then decreased dramatically when the stress surpassed 100 MPa. Crack propagation was the main cause of the decrease in the thermal conductivity, which was related to interphase debonding between the graphite and matrix, and grain boundary sliding. Interphase debonding was related to the creep temperature and stress. Compared to the creep stress, the creep temperature played an important role in the interphase debonding between the graphite and matrix.

<https://doi.org/10.1007/s11661-019-05278-x>

© The Minerals, Metals & Materials Society and ASM International 2019

## I. INTRODUCTION

COMPACTED graphite cast iron (CGI) has excellent tensile strength and heat-transferring properties.<sup>[1,2]</sup> Because of the outstanding mechanical and physical properties, CGI is suitable for complex-shaped components<sup>[3,4]</sup> and has gradually become an essential manufacturing material for advanced engine combustor parts, such as the cylinder head.<sup>[5–8]</sup> With an increase in the power density in engine combustors, the cylinder head endures a high temperature, which requires high-temperature strength and thermal conductivity for thermal fatigue during service.<sup>[9–11]</sup>

Recently, numerous studies have evaluated the mechanical properties and thermal conductivity of cast iron as a material for diesel heads. Selin<sup>[12]</sup> and Qiu<sup>[13]</sup> investigated the tensile property of CGI at elevated temperatures. They showed that the tensile strength initially decreases slowly and then rapidly with an increase in temperature. Microcracks easily initiate at the graphite/matrix interface and then propagate along the graphite, which results in failure. Because of its

brittleness, graphite often contains natural microcracks in the microstructure, negatively affecting the mechanical properties. However, graphite provides an outstanding heat conduction path because of its excellent thermal conductivity. The thermal conductivity of graphite depends on its growth direction, sizes, and shape. Holmgren *et al.*<sup>[14]</sup> estimated the relationship between the graphite growth direction and thermal conductivity of cast iron. They stated that the thermal conductivity of flake graphite is better than that of vermicular graphite followed by nodular graphite, because heat diffuses faster in the *a*-axis direction of graphite than in the *c* axis. Hecht *et al.*<sup>[15]</sup> also showed that the thermal diffusivity of cast iron increases with the size of A type flake graphite. In addition, Ma *et al.*<sup>[16]</sup> and Liu *et al.*<sup>[17]</sup> analyzed the effect of the graphite 3D structure on the thermal conductivity. Ma stated that the thermal conductivity of CGI increases with the vermicularity by an FE model. Liu determined that interconnected graphite in the 3D structure improves the heat conduction of the cast iron when the graphite is less spheroidal.

Moreover, the casting processes and alloying element level can also affect the thermal conductivity. Holmgren *et al.*<sup>[18]</sup> showed linear relationships between the thermal conductivity and carbon content, carbon equivalent, and fraction of pearlite transformed from the former primary solidified austenite. The best thermal conduction property corresponds to a medium cooling rate. Maluf *et al.*<sup>[19]</sup> demonstrated that molybdenum can improve the heat resistance of cast iron, while decreasing the thermal conductivity. Conversely, copper, an excellent heat conductive element, improves heat conduction.

---

WU YUE, LI JIANPING, YANG ZHONG, GUO YONGCHUN, MA ZHIJUN, LIANG MINXIAN, YANG TONG, and TAO DONG are with the Shaanxi Province Engineering Research Centre of Aluminium/Magnesium Light Alloy and Composites, School of Materials and Chemical Engineering, Xi'an Technological University, Xi'an 710021, P.R. China. Contact e-mail: lunwenlj@163.com.

Manuscript submitted November 2, 2018.

Article published online May 22, 2019

Selin *et al.*<sup>[12]</sup> determined that the thermal conductivity of CGI decreases with the silicon content when the carbon equivalent is constant.

A cylinder head operates at a high temperature with accompanying loads, which affects the material's thermal conductivity. However, numerous studies present the effect of the casting processes, alloying elements, and morphologies of the graphite on the thermal conductivity of cast iron. The thermal conductivity variation at an elevated temperature coupled with loads has rarely been systematically analyzed. Therefore, the variation mechanism of the thermal conductivity changing with the temperature and loads should be evaluated.

## II. EXPERIMENTAL PROCEDURE

The chemical composition of experimental CGI is listed in Table I. Pig iron and 45 steel were melted in a GGW-0.01 medium-frequency induction furnace. The molten iron treated by homemade inoculant (75FeSi) and vermiculizer (RE-75-Mg-Ca), respectively, was poured into a sand mold at 1480 °C and produced a wedge-shaped block, as shown in Figure 1. The tensile property of the CGI at different temperatures is shown in Figure 2. The tensile strength of the CGI decreased from 495 to 326 MPa when the temperature increased from room temperature to 450 °C.

The microstructure of the as-cast CGI was observed by an optical microscope, as shown in Figure 3. The main phases of CGI are pearlite, ferrite, and vermicular graphite surrounded by few ferrites. The creep specimens were cut out in “ab,” labeled as in Figure 1, and the diagram of the sample is shown in Figure 4. A creep test was carried out in the RDL100 device and creep temperature was adjusted by the SHIMADEN FP93 instrument. Three N-type thermocouples were bound in the gage regions of the sample. To maintain a parallel position of the specimen to the load direction, an initial load (less than 10 pct of the creep load) was applied during heating. The creep temperature was held for 60 minutes when it reached the target values (350 °C, 450 °C, 500 °C, and 550 °C). Subsequently, different creep stresses were applied on the sample (40, 100, 110, 130, and 150 MPa). The creep temperatures and loads were obtained from previous research.<sup>[20]</sup>

The thermal conductivity testing sample was cut by the electric discharge machine vertical to the stress direction from the gage position of the specimen, as shown in Figure 5. The sample was polished, and the surfaces were covered with a graphite layer, which increased the laser absorption. Then, the thermal conductivity test was carried out in an argon atmosphere. The thermal conductivity testing temperature ranged from 200 °C to 500 °C.

Thermal conductivity of the CGI can be calculated by Eq. [1]<sup>[12,21]</sup>:

$$\lambda = \alpha \rho C_p. \quad [1]$$

Here,  $\lambda$  is the thermal conductivity;  $\alpha$  is the coefficient of thermal diffusion;  $\alpha$  is measured by the Netzsch LFA 457 laser thermal conductivity meter. This process can be described by Eq. [2], where  $\rho$  is the density of the material;  $C_p$  is the specific heat of the test sample and can be calculated according to Eq. [3].

$$\alpha = C \frac{l^2}{t_{0.5}}, \quad [2]$$

$$C_p = \frac{C_{PR} \cdot m_R \Delta T_R}{m_P \Delta T_P}, \quad [3]$$

where  $l$  is thickness of specimen;  $C$  is a constant value, 0.1388;  $t_{0.5}$  is the time for a 50 pct, temperature increase in the testing sample;  $C_{PR}$  is the specific heat of the reference sample;  $m_P$  and  $m_R$  are the quality of the testing sample and referential sample, respectively;  $\Delta T_P$  and  $\Delta T_R$  are the temperature increase of the testing sample and referential sample.

The density of the sample at room temperature was measured by the Mettler Toledo balance. Generally, the density of the material changes with the temperature, as in Eq. [4]:

$$\rho(T) = \frac{\rho}{(1 + \beta \Delta T)^3}, \quad [4]$$

where  $\Delta T$  is the temperature increase and  $\beta$  is the linear coefficient of thermal expansion,  $14.5 \times 10^{-6} \text{ K}^{-1}$ . Because of the slight variation in the density, the density of the sample was considered a constant value in this study.

A metallographic specimen was cut from the sample after the creep test by the electric discharge machine along the direction of the creep stresses, polished by SiC abrasive paper (240×, 600×, 1000×, 1500×, 2000×), and then etched by 4 pct Nital solution. The metallographic specimen was observed by scanning electron microscopy (SEM, Tescan VEGA-II XMU). Energy dispersive spectroscopy (EDS) was also used to analyze the distribution of the elements during observation. The creep temperature is different from the thermal conductivity testing temperature in this study. The former is the creep test temperature. When the creep test is complete, the thermal conductivity test is performed at different testing temperatures (from 200 °C to 550 °C).

## III. RESULTS

### A. Thermal Conductivity of CGI

#### 1. Thermal conductivity vs creep temperature

The thermal conductivity vs the creep temperature under 150 MPa at different thermal conductivity testing temperatures is shown in Figure 6. The thermal conductivity of CGI decreases with the testing temperature. As the testing temperature increases, the thermal conductivity decreases by approximately 6 to 10 pct. In addition, the variation tendency of the thermal

**Table I. Chemical Composition of Experimental CGI (Mass Fraction, Percent)**

| Element    | C   | Si  | Mn  | Cu   | Mo  | Sn   | P      | S         | Fe   |
|------------|-----|-----|-----|------|-----|------|--------|-----------|------|
| Percentage | 3.9 | 1.8 | 0.2 | 0.55 | 0.2 | 0.03 | < 0.06 | 0.02–0.03 | bal. |

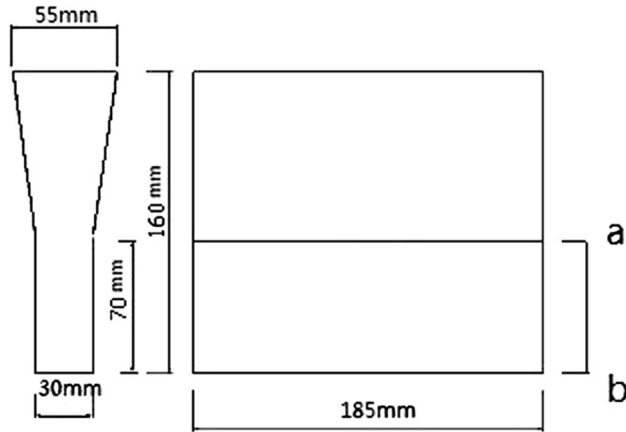


Fig. 1—Schematic diagram of wedge-shaped block of CGI.

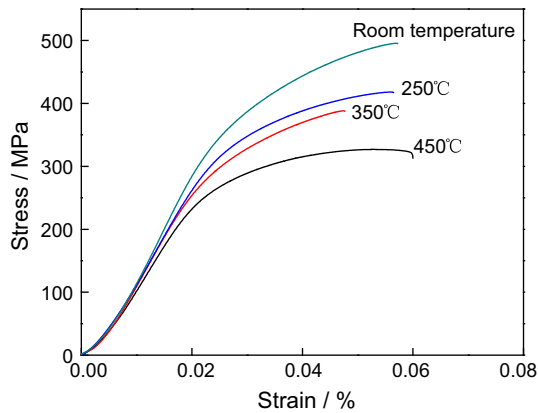


Fig. 2—Tensile property of CGI at different temperatures.

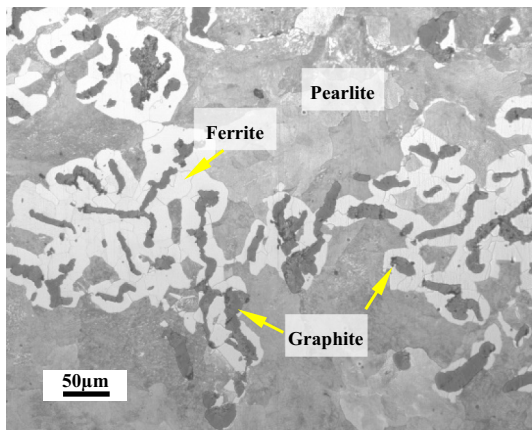


Fig. 3—As-cast microstructure of CGI.

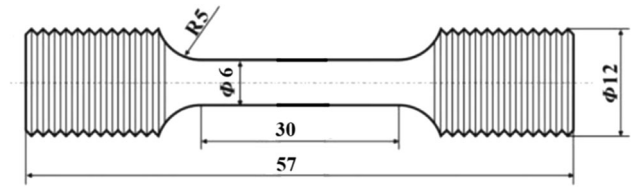


Fig. 4—Schematic diagram of creep test sample.

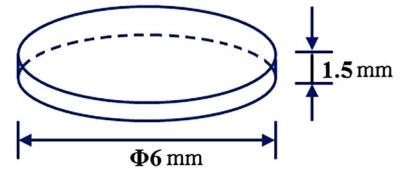


Fig. 5—Schematic diagram of thermal conductivity test sample.

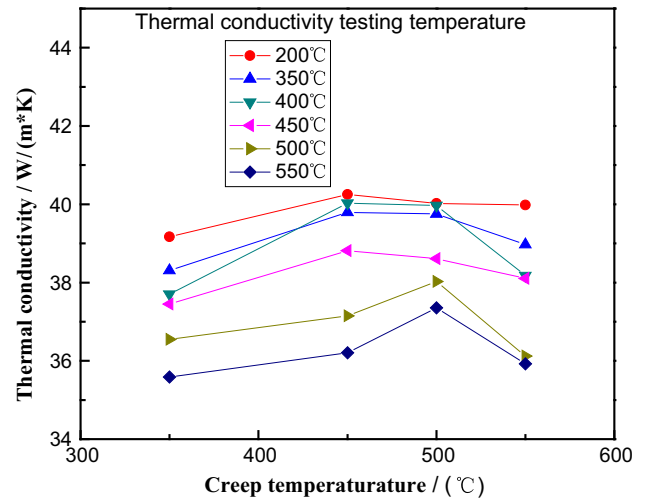


Fig. 6—Thermal conductivity of CGI vs the creep temperature under 150 MPa.

conductivity with the creep temperature presents two stages. First, the thermal conductivity slightly increases with the creep temperature, from approximately 350 °C to 500 °C. Then, the thermal conductivity dramatically decreases when the creep temperature increases to 550 °C.

### 2. Thermal conductivity vs creep stress

The thermal conductivity vs the creep stress of CGI at 550 °C is shown in Figure 7. The variation tendency of the thermal conductivity with the creep stress presents two stages. First, the thermal conductivity slightly decreases when the creep stress increases from 40 to 100 MPa and then greatly fluctuates and descends dramatically when the creep stress surpasses 100 MPa,

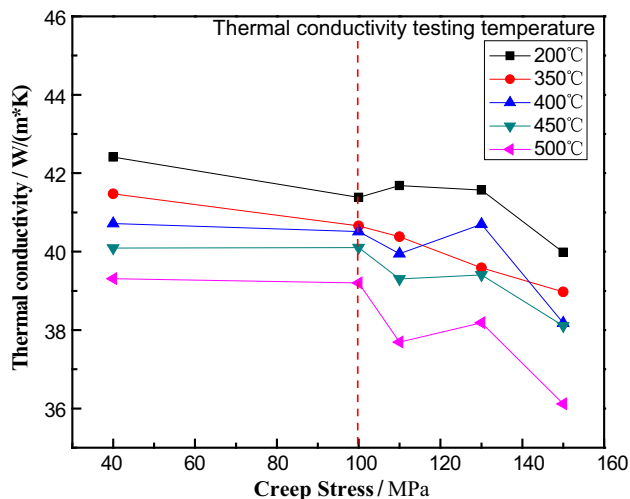


Fig. 7—Thermal conductivity of CGI vs the creep stress at 550 °C.

**Table II. Creep Test Results at Different Temperatures**

| Load/MPa | Dwell Time/h |        |        |                |
|----------|--------------|--------|--------|----------------|
|          | 350 °C       | 450 °C | 500 °C | 550 °C         |
| 40       | —            | —      | —      | 100            |
| 100      | —            | —      | —      | 100            |
| 110      | —            | —      | —      | 75 (fracture)  |
| 130      | —            | —      | —      | 22 (fracture)  |
| 150      | 100          | 100    | 100    | 9.5 (fracture) |

which may be related to the microstructure damages caused by the large stress.

## B. Evolution of the Microstructure and Damage

### 1. Pearlite decomposition

The creep testing results are listed in Table II. The specimen was maintained for 100 hours without failure from 350 °C to 500 °C under 150 MPa. However, it fractured quickly at 550 °C, demonstrating that the CGI strength decreases. The microstructure of the CGI after the creep test at 40 MPa and 550 °C for 100 hours is shown in Figure 8. Most of the graphite is vermicular graphite (VG). The remainder is nodular graphite (NG). The pearlite transforms to carbon and ferrite at high temperature, and its lamellar structure fades gradually, as shown in the yellow circle in Figure 8(a). Eventually, the pearlite morphology is short and small. In addition, the morphologies of the pearlite vary based on the positions. For example, the pearlite near the grain boundary contains a granular shape, especially near the VG/pearlite phase boundary; however, a lamellar structure forms in the interior pearlite grain, as shown in Figure 8(b), because the decomposition rate near the vermicular graphite is faster than that in the interior grain. As the vermicular graphite has a larger specific surface area than that of nodular graphite, carbon can diffuse to the adjacent graphite easily when its solubility in ferrite is saturated.

### 2. Microstructure damage evolution

Various morphologies of graphite debonding after the creep test are observed by SEM, as shown in Figure 9. There are two types of graphite debonding observed in the microstructure. The specimen is broken and interfacial debonding occurs at the interface between the graphite and matrix, as shown in Figure 9(a), when the stress surpasses the ultimate tensile strength (495 MPa) at room temperature. Interphase debonding becomes more evident after the creep test at 450 °C for 100 h under 150 MPa, which could be related to the different mechanical properties and mismatched deformation between the graphite and matrix, as shown in Figure 9(b). At 40 MPa and 500 °C for 100 hours, interphase debonding becomes evident between the interface of the nodular graphite and matrix, as shown in Figure 9(c), although there is a lower stress concentration in the tip of nodular graphite compared to that of vermicular graphite. Thus, the creep temperature plays an important role in interphase debonding compared to the creep stress. This phenomenon is similar to our previous study.<sup>[22]</sup> Interphase debonding also occurs without any external loads at a high temperature, owing to the thermal stress difference at the interface between the graphite and matrix caused by the different thermal properties. In addition, interlamellar debonding within the graphite lamellar structure is observed, as shown in Figure 9(d), particularly in the oxidation parts, which may be related to the graphite bond force decline caused by oxidation. Thus, the main damage generated in the microstructure of CGI is graphite debonding between the matrixes.

## IV. ANALYSIS AND DISCUSSION

### A. Graphite Debonding

According to the study by Rukadikar,<sup>[23]</sup> graphite is the best heat conduction path followed by ferrite and pearlite in the microstructure of CGI (the thermal conductivities of graphite, ferrite, and pearlite are 130 W/(m\*K), 80 W/(m\*K), and 50 W/(m\*K), respectively). However, there are two models of graphite debonding: (I) interphase debonding and (II) inter-laminar debonding, as concluded in Section III-A, which decreases the efficiency of heat conduction.

Interphase debonding is widespread owing to the deformation mismatch between graphite and the matrix. Normally, interphase debonding occurs with the help of the tensile stress. When the load is equal to the tensile strength, the specimen is fractured. Because ductile than pearlite, obvious deformation occurs in ferrite, as shown in Figure 9(a). Therefore, interphase debonding between graphite and ferrite is greater than that between graphite and pearlite, as shown in Figure 9(b). In addition, interphase debonding can also occur between the different phases at high temperature because of the different thermal and physical properties. This result is shown in our previous research.<sup>[22]</sup> Under the combination effect of the tensile stress and high temperature, interphase debonding occurs easily and obviously. The



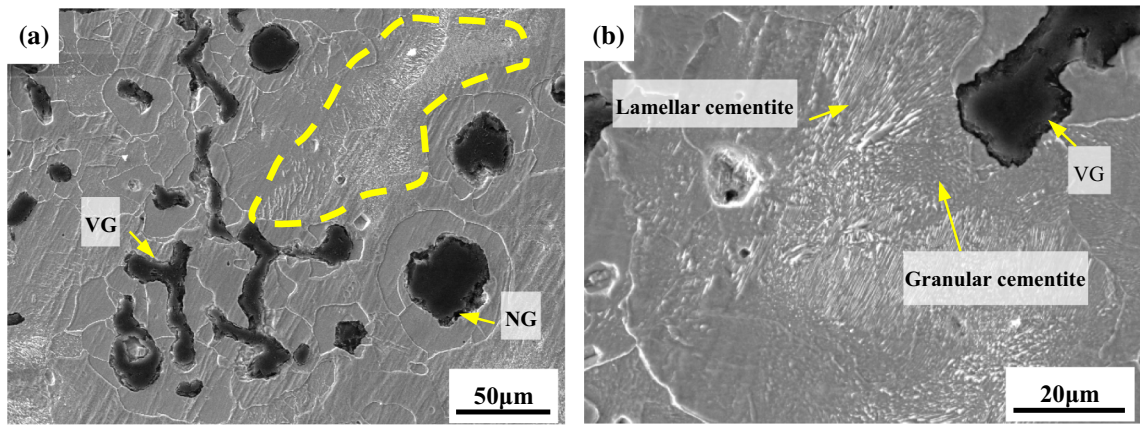


Fig. 8—Microstructure of CGI at 550 °C for 100 h under 40 MPa: (a) pearlite decomposing and (b) pearlite presents lamellar in the interior pearlite grain and granular near the VG.

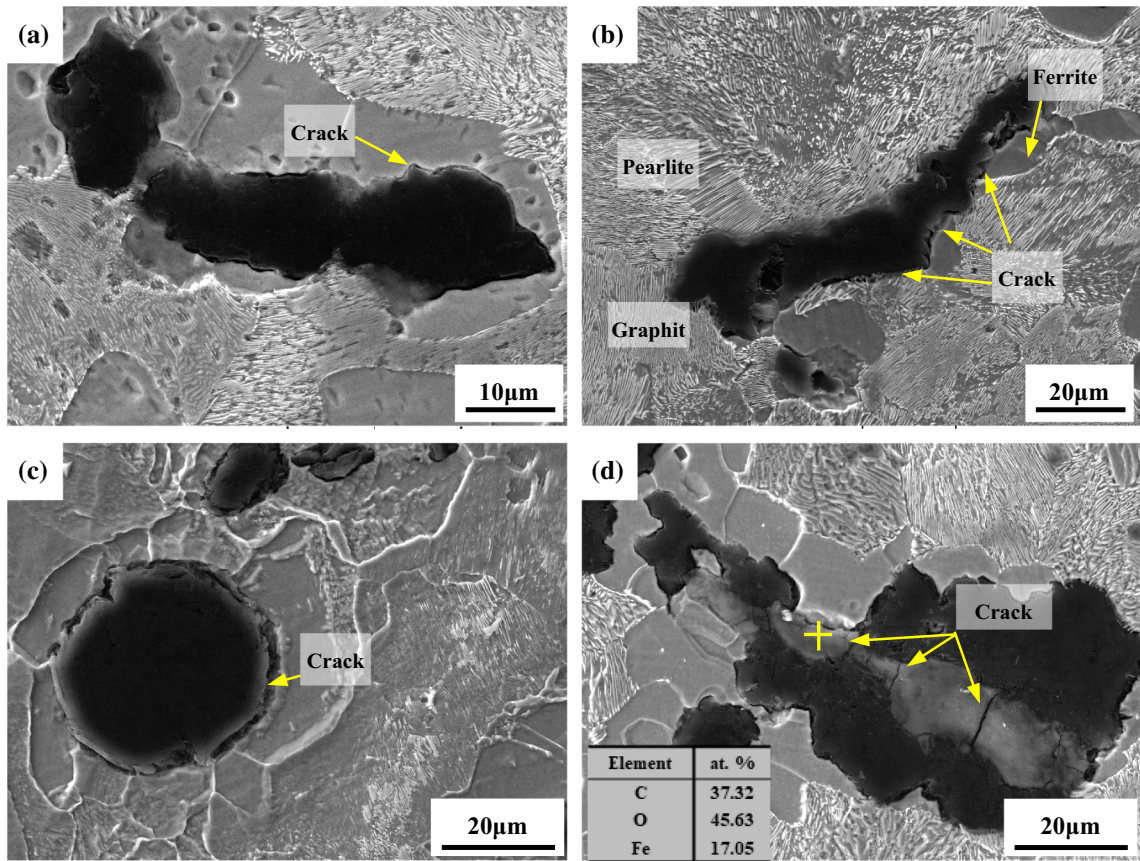


Fig. 9—Graphite debonding: (a) fractured microstructure at room temperature (up to the tensile strength); (b) 450 °C, 150 MPa for 100 h; (c) 500 °C, 40 MPa for 100 h; and (d) internal VG oxidation at 450 °C and 150 MPa for 100 h.

creep temperature plays a more important role than the creep stress because interphase debonding occurs more easily at a higher temperature even under a lower stress, as shown in Figures 9(b) and (c).

In addition, interlamellar debonding will occur during the creep test. There are obvious microcracks in graphite, especially in the oxidation zones, as shown in Figure 9(d). The oxidized cracks will decrease the heat conduction efficiency. Normally, oxygen atoms can

diffuse in the microstructure through vermicular graphite because of its 3D connectivity, and graphite can easily oxidize at a high temperature. If the connectivity is greater, the graphite net channel will flourish. However, the oxygen atoms can also diffuse in the graphite channel quickly and cause graphite oxidation. Therefore, the higher 3D connectivity cannot result in a favorable thermal conductivity at a high temperature because of graphite oxidation. The relationship between

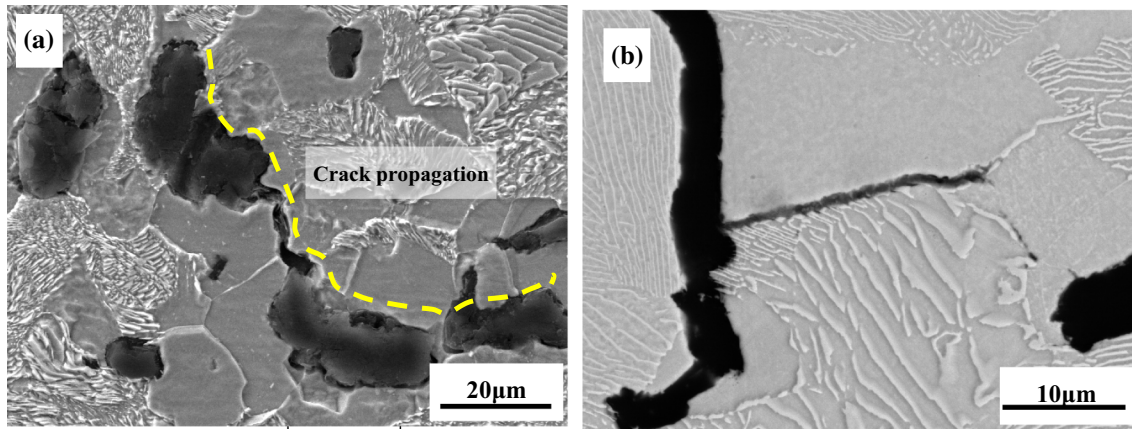


Fig. 10—Crack propagation hinders heat diffusion: (a) crack propagation through ferrite originated from the graphite debonding tip and (b) intergranular crack between ferrite and pearlite.

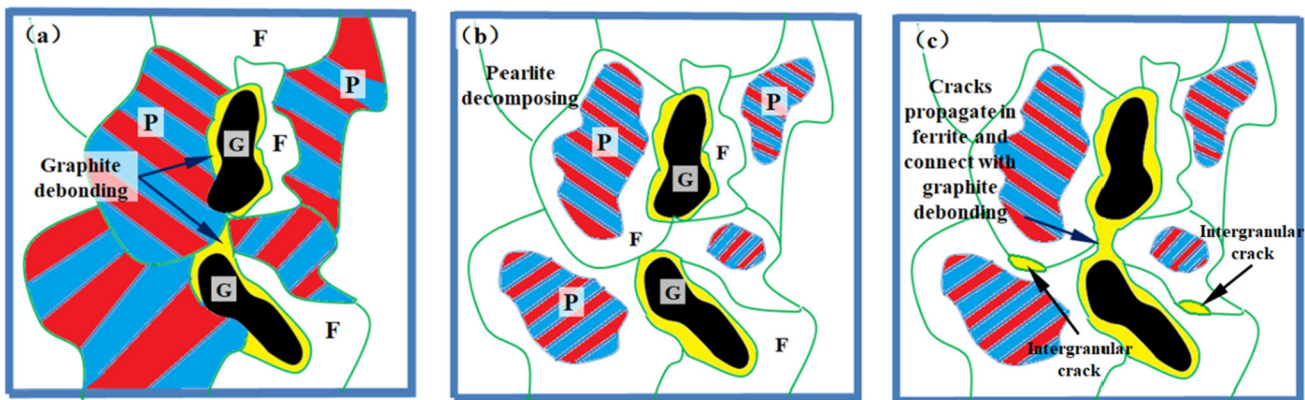


Fig. 11—Thermal conductivity mechanism of CGI during the creep test: (a) graphite debonding occurs under stress at high temperature; (b) pearlite decomposing and graphite debonding is obvious and (c) cracks propagate in ferrite and connect with graphite debonding, meanwhile, intergranular crack occurs in the boundary.

oxidation and the cracks in graphite requires further research.

### B. Thermal Conductivity Affected by Microstructure Evolution and Damage

As shown in Figure 6, there are two stages in the curve of the thermal conductivity values *vs* the creep temperature: (I) a slight increase from 350 °C to 500 °C and (II) a dramatic decrease from 500 °C to 550 °C. This change is related to the microstructure evolution and damage.

When the creep temperature increases from 350 °C to 500 °C, the thermal conductivity increases slightly, which is related to the pearlite decomposition at a high temperature. Cementite in the pearlite will transform to ferrite and carbon. The latter can diffuse to the adjacent graphite and cause a rough surface.<sup>[24]</sup> The connectivity and vermicularity are nearly constant. Therefore, the contribution to the thermal conductivity increase caused by the carbon atoms diffusing into the graphite can be neglected, and the improvement of the heat conduction is owing to the increasing content of ferrite. During the creep test, pearlite decomposition occurs with graphite

debonding. The former promotes thermal conductivity, while the latter hinders it. The thermal conductivity increases slightly because pearlite decomposition is prior to graphite debonding when the creep temperature increases to 500 °C.

When the creep temperature increases to 550 °C, the thermal conductivity of CGI decreases dramatically, which is related to the microstructure damage. The microcrack will initiate easily at the tip of interphase debonding, and then it will propagate through the ferrite preferentially. According to the study by Zhang,<sup>[10]</sup> the threshold of the fatigue crack growth of pearlite is higher than that of ferrite; therefore, the crack can expand in ferrite easily. Microcracks in ferrite will connect adjacent interphase debonding. Microcracks will grow and run through the specimen by the action of the bridge connection, as shown in Figure 10(a). The cracks in the grain boundary can also decrease the thermal conductivity. According to the study by Qiu,<sup>[13]</sup> the strength of the CGI change with the temperature presents two stages. When the temperature is lower than 450 °C, dislocation movement inhibition is the main deformation mechanism. Because of strain hardening,



dynamic strain aging (DSA effect), and precipitation strengthening, the strength of the CGI will decrease gradually. However, when the temperature surpasses 450 °C, ferrite boundary sliding becomes active, which causes intergranular cracks and widespread holes in the grain boundary. Our previous research also showed this damage model,<sup>[20]</sup> as shown in Figure 10(b). Therefore, the cracks propagating through ferrite originate from the graphite debonding tip, and the intergranular cracks decrease the thermal conductivity.

In addition, the thermal conductivity decreases with an increase of the creep stress, as shown in Figure 7. This is because less damage is generated under lower stress, and the specimen is sustained for a long time at a high temperature, which induces more pearlite decomposition. Therefore, the thermal conductivity of CGI decreases with the increment of the loads at 550 °C.

### C. Mechanism of the Thermal Conductivity of CGI During the Creep Test

Ghodrat<sup>[1]</sup> pointed out that TMF (thermal mechanical fatigue) life of CGI mainly depends on crack propagation instead of crack initiation. Since internal graphite particles act as natural notches, interphase debonding initiates immediately at the tip of graphite when fatigue loops start. Our research also demonstrates this result, as shown in Figure 9. Therefore, it can be concluded that the interface between graphite and matrix will be debonding firstly at creep initial stage. Because of low creep temperature (450 °C), pearlite decomposition is not obvious. When creep temperature rises to 500 °C, pearlite decomposition becomes severe and interphase debonding is obvious. When the effect of pearlite decomposition on thermal conductivity surpasses that of interphase debonding, thermal conductivity of CGI increases slightly. When creep temperature increases further (550 °C), microstructure damage becomes serious. On the one hand, cracks will propagate through ferrite originated from interphase debonding tip. On the other hand, intergranular cracks will be widespread in the ferrite boundary because of active grain boundary sliding. Both can hamper heat conduction. Hence, thermal conductivity of CGI decreases dramatically.

The variation in the thermal conductivity is affected by the creep temperature and stress. The process of the thermal conductivity of the CGI influenced by the creep temperatures and loads can be explained in three steps, as described in Figure 10. First, graphite debonding occurs easily at a high temperature, as shown in Figure 11(a), which spreads heat through the matrix mainly consisting of pearlite. Because of the minimal pearlite decomposition, the thermal conductivity decreases. As the pearlite decomposes gradually with an increase of the creep temperature, the thermal conductivity increases slightly, as described in Figure 11(b). However, when the crack preferentially propagates through ferrite and connects with graphite/matrix debonding, the heat conduction path is broken. Meanwhile, the intergranular crack in the grain boundary affected by the boundary sliding will

also decrease the thermal conductivity. Finally, the thermal conductivity decreases, as shown in Figure 11(c).

## V. CONCLUSIONS

- (1) The thermal conductivity of the CGI increased gradually at first, and then decreased with the creep temperature under 150 MPa. At 550 °C, the thermal conductivity decreased gradually at first, and then decreased dramatically when the creep stress surpassed 100 MPa, which was related to the internal damage evolution.
- (2) Two types of graphite debonding were observed in the microstructure: (I) interphase debonding, which occurred at the interface between the graphite and matrix and (II) inter-laminar graphite debonding within its laminar structure. Both can decrease the thermal conductivity. Compared to the stress, the creep temperature presented a dominate role in the interphase debonding between the graphite and matrix.
- (3) Crack propagation through the ferrite preferentially originated from the interphase debonding tip and intergranular crack in the ferrite boundary because of the boundary sliding that could hinder heat conduction and decrease the thermal conductivity. This caused the thermal conductivity to decrease during the creep test.

## ACKNOWLEDGMENTS

The authors would like to acknowledge financial support by Key Project of Equipment Pre-research Field Fund (6140922010301), Key Research Program of Shaanxi Provincial Department of Technology and Science (2018ZDXM-GY-137), Key Research and Development Plan of Shaanxi Province (2018GY-176), Shaanxi creative talents promotion plan-technological innovation team (2017KCT-05), and National Basic Science Development Foundation of China (61322402).

## REFERENCE

1. S. Ghodrat, T.A.C. Riemslag, A.I. Kestens, and J. Sietsma: *Metall. Mater. Trans. A*, 2013, vol. 44A (5), pp. 2121–30.
2. Q. Guo, Z. Yang, D. Tao, P.H. Gao, Y.C. Guo, and J.P. Li: *J. Alloy. Compd.*, 2018, vol. 765, pp. 213–20.
3. T. Yang, Y.C. Guo, J.P. Li, Z.Z. Chen, and W. Zhang: *Foundry*, 2008, vol. 57, pp. 270–73.
4. Z. Yang, D. Tao, Y.C. Guo, T. Yang, and J.P. Li: *Foundry*, 2014, vol. 63, pp. 115–19.
5. Y. Wu, J. Li, Z. Yang, Y.C. Guo, Z.J. Ma, M.X. Liang, T. Yang, and D. Tao: *Chin. J. Mater. Res.*, 2019, vol. 33 (01), pp. 43–52.
6. Z.J. Ma, Q. Wen, P.H. Gao, Z. Yang, Y.C. Guo, J.P. Li, and M.X. Liang: *Int. J. Cast Metals Res.*, 2018, vol. 31 (4), pp. 230–36.
7. Z.F. Zhang, Y.Y. Zhang, J.C. Pang, R.L. Shen, Y. Qiu, and S.X. Li: *Mater. Sci. Eng. A*, 2018, vol. 713, pp. 260–68.
8. S. Dawson: *Foundry Technol.*, 2009, vol. 30, pp. 455–60.

9. B. Fedelich, H. Kühn, B. Rehmer, and B. Skrotzki: *Int. J. Fatigue*, 2017, vol. 99, pp. 266–78.
10. M.X. Zhang, J.C. Pang, Y. Qiu, S.X. Li, M. Wang, and Z.F. Zhang: *Mater. Sci. Eng. A*, 2017, vol. 698, pp. 63–72.
11. V. Norman, P. Skoglund, D. Leidermark, and J. Moverare: *Int. J. Fatigue*, 2015, vol. 80, pp. 381–90.
12. M. Selin and M.K. Nig: *Metall. Mater. Trans. A*, 2009, vol. 40A, pp. 3235–44.
13. Y. Qiu, J.C. Pang, E.N. Yang, E.N. Yang, W.Q. Fu, M.X. Liang, and Z.F. Zhang: *Mater. Sci. Eng. A*, 2016, vol. 677, pp. 290–301.
14. D. Holmgren, K.R. Ilbom, and I.L. Svensson: *Metall. Mater. Trans. A*, 2007, vol. 38A, pp. 268–705.
15. R.L. Hecht, R.B. Dinwiddie, and H. Wang: *J. Mater. Sci.*, 1999, vol. 34, pp. 4775–78.
16. Z.J. Ma, D. Tao, Z. Yang, Y.C. Guo, and J.P. Li: *Mater. Des.*, 2016, vol. 93, pp. 418–22.
17. Y. Liu, W. Li, Y. Li, J. Xing, S. Wang, B. Zheng, and D. Tao: *Mater. Charact.*, 2018, vol. 144, pp. 155–65.
18. D. Holmgren, A. Diószegi, I.L. Svensson: *China Foundry*, 2007, pp. 210–14.
19. O. Maluf, M. Angeloni, D. Castro, W. Filho, D. Spinelli: *J. Mater. Eng. Perform.*, 2009, pp. 980–84.
20. Y. Wu, J. Li, Z. Yang, Z. Yang, Y.C. Guo, Z.J. Ma, M.X. Liang, and D. Tao: *Mater. Sci. Eng. A*, 2018, vol. 723, pp. 174–81.
21. T. Ying, M.Y. Zheng, Z.T. Li, X.G. Qiao, and S.W. Xu: *J. Alloys Compds.*, 2015, vol. 621, pp. 250–55.
22. Y. Wu, J.P. Li, Y.J. Zhang, Z. Yang, D. Tao, and T. Yang: *Trans. Mater. Heat Treat.*, 2017, vol. 38, pp. 143–51.
23. M.C. Rukadikar and G.P. Reddy: *J. Mater. Sci.*, 1986, vol. 21, pp. 4403–10.
24. Y. Qiu, J.C. Pang, S.X. Li, E.N. Yang, W.Q. Fu, M.X. Liang, and Z.F. Zhang: *Mater. Sci. Eng. A*, 2016, vol. 664, pp. 75–85.

**Publisher's Note** Springer Nature remains neutral with regard to jurisdictional claims in published maps and institutional affiliations.